Nanocrystalline Structure and Thermoelectric Properties of Electrospun $NaCo_2O_4$ Nanofibers

Feiyue Ma,[†] Yun Ou,[‡] Yang Yang,[†] Yuanming Liu,[†] Shuhong Xie,[†,‡] Jing-Feng Li,[§] Guozhong Cao,[∥] Roger Proksch,[⊥] and Jiangyu Li*[,†]

Department of Mechanical Engineering, University of Washington, Seattle, Washington 98195-2600, United States, Key Laboratory of Low Dimensional Materials and Application Technology of Ministry of Education, and Faculty of Materials, Optoelectronics and Physics, Xiangtan University, Hunan, 411105, P. R. China, State Key Laboratory of New Ceramics and Fine Processing, and Department of Materials Science and Engineering, Tsinghua University, Beijing, 100084, P. R. China, Department of Materials Science and Engineering, University of Washington, Seattle, Washington 98195-2120, United States, and Asylum Research, 6310 Hollister Ave., Santa Barbara, California 93117, United States

Received: August 9, 2010; Revised Manuscript Received: November 8, 2010

High-efficiency thermoelectric oxide materials are promising for the conversion of waste heat directly into electricity, and nanostructure engineering is effective in enhancing thermoelectric figure of merit through phonon scattering at grain boundaries and interfaces. In this work, we report a sol−gel-based electrospinning technique to synthesize thermoelectric $NaCo_2O_4$ nanofibers with grain size as small as 10 nm, orders of magnitude smaller than that of $NaCo_2O_4$ powders processed by conventional sol−gel techniques. A series of scanning probe microscopy (SPM) studies are carried out to measure the electric conduction in a single $NaCo_2O_4$ nanofiber, and the thermoelectric effect of a single $NaCo_2O_4$ nanofiber is also characterized using a novel thermal probing technique that induces a large temperature gradient in the nanofiber. Sintering of nanocrystalline nanofibers into bulk $NaCo_2O_4$ ceramics for thermoelectric energy harvesting is also discussed.

1. Introduction

Meeting the ever-increasing global energy needs in an environmentally and geopolitically sustainable manner is one of the most pressing technological challenges today. Currently, about 34% of world primary energy needs are supplied by petroleum, and a large portion of petroleum energy are consumed for transportation.[1] For a vehicle powered by a typical gasoline-fueled internal combustion engine, the vast majority of the fuel energy is lost as waste heat − only 25% of the fuel energy is used for vehicle mobility and accessory power.[2] This points to an urgent need for alternative energy technology to harvest the waste heat in an efficient, economical, and environment friendly manner, and high-efficiency thermoelectric materials that convert waste heat directly into electricity are promising to fulfill this need.

Thermoelectric energy conversion efficiency is governed by thermoelectric figure of merit *ZT*, which is intimately related to electric and thermal transport properties of thermoelectric materials.[3,4] High-efficiency thermoelectric conversion requires simultaneously high electric conductivity and low thermal conductivity, and this turns out to be rather challenging, because in most materials high electric conductivity is usually accompanied by high thermal conductivity. In fact, the electron contribution of thermal conductivity is proportional to electric conductivity according to the Wiedemann−Franz Law, and, as a result, reducing phonon contribution to thermal conductivity is the remaining option for enhancing thermoelectric conversion efficiency. This could be realized by exploiting phonon scattering at boundaries and interfaces to reduce thermal conduction by phonons, for which engineered nanostructures are very effective due to their substantially increased interfaces. Indeed, many nanostructured thermoelectrics have been explored, including low-dimensional materials such as nanowires, nanotubes, and superlattices,[5−15] and bulk thermoelectrics with nanostructured constituents, such as nanocrystalline materials and nanocomposites.[11,16−22]

Encouraged by these developments and our recent works on nanocrystalline multiferroic nanofibers,[23−25] we have developed a sol−gel-based electrospinning technique to synthesize nanocrystalline thermoelectric oxide nanofibers[26] with a grain size as small as 10 nm. Compared to single crystalline nanowires, the nanocrystalline nanofibers offer additional advantages in phonon scattering at grain boundaries, and thus their thermal conductivity could be substantially reduced even further. For automobile applications involving waste heat from combustion engine, thermoelectrics must be composed of nontoxic materials with good chemical stability in air and at temperature up to 800−1000 K, and oxide thermoelectrics offer such attractive characteristics. Among potential oxide materials, layered cobalt oxides, such as $NaCo_2O_4$, $Ca_3Co_4O_9$, and $Bi_2Sr_2Co_2O_x$ are particularly promising for thermoelectric applications.[27−31] They are layered materials consisting of complex crystalline structure, similar to artificially engineered superlattices, in which CoO_2 nanosheets possessing a strongly correlated electron system serve as electronic transport layers, whereas sodium ion nanoblock layers, calcium, or strontium cobalt oxide misfit layers

* To whom the correspondence should be addressed. Tel: 206-543-6226. Fax: 206-685-8047. E-mail: jjli@u.washington.edu.
† Department of Mechanical Engineering, University of Washington.
‡ Key Laboratory of Low Dimensional Materials and Application Technology of Ministry of Education, and Faculty of Materials, Optoelectronics and Physics, Xiangtan University.
§ State Key Laboratory of New Ceramics and Fine Processing, and Department of Materials Science and Engineering, Tsinghua University.
∥ Department of Materials Science and Engineering, University of Washington.
⊥ Asylum Research.

10.1021/jp107488k
Published on Web 12/02/2010

serve as phonon scattering regions. As a result, it is possible to control and optimize electron and phonon transports separately, and thus enhance their thermoelectric figure of merit. Indeed, *ZT* value as high as 1.2 has been observed in $NaCo_2O_4$ single crystal,[32] and for polycrystalline $NaCo_2O_4$, a *ZT* value of 0.8 has been reported.[32,33]

$NaCo_2O_4$ is particularly suitable for nanocrystalline engineering because its thermal transport is dominated by phonons − the thermal conductivity of NaCo2O4 crystal is measured to be 19 W/(m·K), among it 16.5 W/(m·K) is contributed by phonons, and only 2.5 W/(m·K) is contributed by charge carriers.[32,33] This points to a possibility of drastic reduction in thermal conductivity by phonon scattering at grain boundaries without reducing its electric conductivity, and for this potential to be fully realized, it is imperative to reduce its grain size to 10−20 nm, which we seek to achieve using sol−gel-based electrospinning.

2. Experimental Methods

2.1. Materials Synthesis. The synthesis method is similar to the work of Maensiri and Nuansing.[26] The precursor solution of $NaCo_2O_4$ was prepared by dissolving cobalt(II) acetate tetrahydrate (Aldrich, reagent grade) and sodium acetate trihydrate (Baker, reagent grade) into methanol or distilled water, with the mole ratio of Na:Co controlled at 1.1:2. The concentration of $NaCo_2O_4$ in methanol and water was set to be 0.15 mol/L and 0.4 mol/L respectively, and the solution was stirred at room temperature for 30 min after mixing the solvent and salts. Polyvinylpyrrolidone (PVP) with molecular weight of 1 300 000 and concentration of 0.1 g/mL was then added into the precursor solution and stirred until a homogeneous polymer solution was formed. The polymer solution was loaded into a plastic syringe, and driven by a syringe pump (NE-500, New Era Pump Systems, Inc.) at a rate of 0.1 mL/h through a 23 gauge stainless steel needle. The needle was connected to a high-voltage power supply (ES40P-5W, Gamma High Voltage, Inc.), with voltage set to be approximately 10 kV and 15 kV for methanol- and water-based solutions. The nanofibers spun were collected on a substrate placed between two parallel grounded stainless steel bars, with the distance between the collector and the tip of the needle set to be approximately 10 cm. The collected nanofibers were dried at 60 °C for methanol-based system and 120 °C for water-based system for at least 1 h to evaporate the solvent, and then transferred into an oven that was preheated to 750 °C and were annealed there for 2 h before being cooled down in the oven. $NaCo_2O_4$ powders were also prepared for comparison using conventional sol−gel method. The precursor sol was dried at 80 °C for 2 days to form a gel, and then annealed using the same method described above to obtain $NaCo_2O_4$ powders.

2.2. Structure Characterization. The morphology of nanofibers was examined by scanning electron microscopy (SEM, FEI Sirion). The SEM sample was collected during a 2 min electrospinning process as described in materials synthesis, and all the samples were sputtered for 60 s to coat a good conductive gold layer of approximately 7 nm thick to enhance the contrast. The crystalline structure of nanofibers was examined by X-ray diffraction (XRD, Bruker D8 Focus) and transmission electron microscopy (TEM, FEI Tecnai). The XRD samples were collected under electrospinning for extended period of time, and were grounded into fine powder after annealing for XRD. For TEM observation, a few nanofibers were transferred onto a TEM grid and then annealed before TEM.

2.3. SPM Characterization. The electric and thermoelectric characterizations were carried out using Asylum Research MFP-3D atomic force microscopy (AFM). The electrical conductivity study was carried by conductive atomic force microscopy (Asylum ORCA module) with a Pt-coated tip (OMCL-AC240TM). Contact scanning mode was used for current mapping, with a biased voltage applied between the tip and substrate. To derive the I−V curve, the tip was fixed at a certain position, and a triangle wave of voltage was applied as bias. The thermoelectric studies were carried out using a "U"-shaped probe with a resistive heater at the end of the cantilever (ThermaLever Probes, AN2−200, Anasys Instruments Corp). The resistor was made of selectively doped silicon, which can locally heat the sample surface at the point of contact with a rapid heating rate. The thermoelectric response was examined using noncontact electrostatic force microscopy (EFM) mode. During the scanning at each point, the surface topography of the sample was measured first without applying any voltages. The sample was then heated locally by applying a heating voltage through the resistor in the tip to create a large temperature gradient, and a bias voltage was simultaneously applied for EFM measurement. All of the voltages were then turned off, and after a short time to allow the sample to cool down, the tip moved to next point, and the process was repeated.

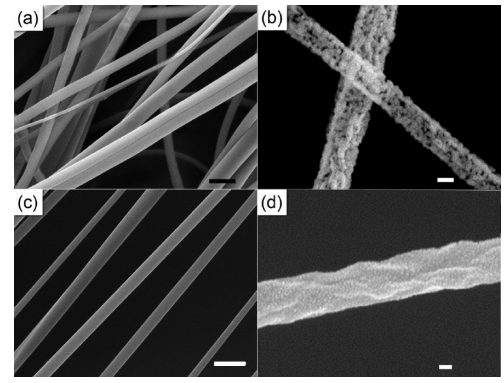

Figure 1. SEM image of $NaCo_2O_4$ nanofibers before and after annealing, synthesized with two different solvents; (a) and (b) methanol-based nanofibers before (a) and after (b) annealing; (c) and (d) water-based nanofibers before (c) and after (d) annealing; scale bars in (a) and (c) represent 1 μm, and in (b) and (d) represent 100 nm.

3. Results and Discussion

Two different solvents were used to prepare the precursor solution of $NaCo_2O_4$, and the morphology of the resulted nanofibers before and after calcination was examined by scanning electron microscopy (SEM), as shown in Figure 1. The nanofibers are straight with smooth surface before calcination, and the diameter of the nanofiber is uniform throughout its length, though there are some variations from fiber to fiber. After calcination, the polyvinylpyrrolidone (PVP) polymers in the nanofibers are burned out, the surfaces of nanofibers become rough, and the diameter of the nanofibers shrinks to about 200 nm. Nevertheless, most nanofibers are able to keep their continuous fibrous morphology. The difference between calcinated nanofibers synthesized using different solvents is also evident − methanol-based nanofibers appear to be porous, and are easy to break, whereas water-based nanofibers appear to be rather dense and robust.

The crystalline structures of both types of calcinated nanofibers are examined by XRD, and are compared with that of sol−gel powders, as shown in Figure 2. All samples show predominantly γ-phase $NaCo_2O_4$ with good crystallinity, with XRD peaks for nanofibers much sharper than those of sol−gel

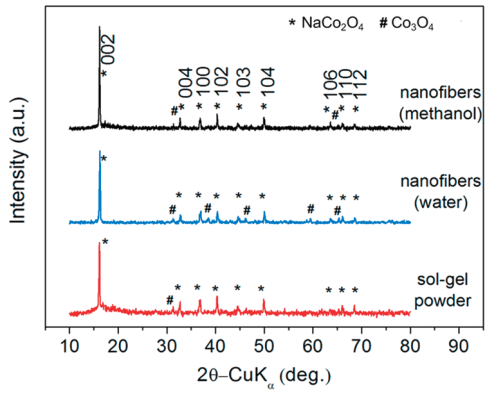

Figure 2. X-ray diffraction patterns of $NaCo_2O_4$ nanofibers and sol−gel powders prepared with methanol and water as the solvent.

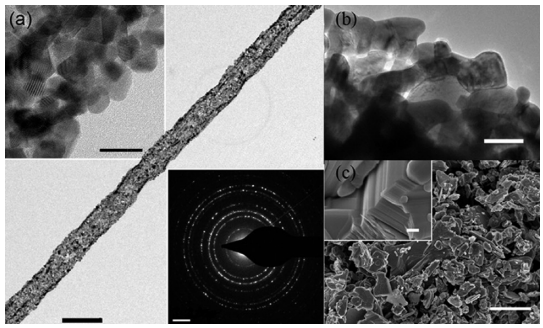

Figure 3. Grain size of $NaCo_2O_4$ nanofiber and sol−gel powders; (a) TEM image of a single nanofiber (scale bar represents 500 nm), with the inserts showing the fine grain size (scale bar represents 20 nm) and SAED ring pattern (scale bar represents 2 nm^{-1}); (b) TEM image of sol−gel powders showing much larger grain size (scale bar represents 200 nm); (c) SEM image of sol−gel powders (scale bar represents 5 μm), with the insert showing large lamellar structure (scale bar represents 200 nm).

powders, especially for methanol-based nanofibers. A small portion of Co_3O_4 phase appears in nanofibers, probably due to sodium evaporation during calcination. The crystalline structure of the nanofiber synthesized using water solvent is further examined by TEM as presented in part a of Figure 3, which shows a nanofiber with large aspect ratio, straight over a large period of length, and having rather uniform cross section and crystallinity throughout the length. The grain size of the nanofiber is in the range of 10−15 nm, as clearly seen in the top-left insert, and selected area electron diffraction (SAED) ring pattern indicates the random orientation distribution of grains in the nanofiber. In contrast, the sol−gel processed powders have much larger grain size well over 200 nm, as shown in part b of Figure 3, and the corresponding SEM image in part c of Figure 3 reveals the lamellar crystalline morphology of $NaCo_2O_4$ powders expected from the layered lattice structure, with the typical lamellar size over 500 nm and can be as large as several micrometers. This suggests that the electrospinning is indeed a very effective method to synthesize nanocrystalline thermoelectric oxides, capable of producing extremely fine grain size that is orders of magnitude smaller than conventional sol−gel process, and thus could result in substantially reduced thermal conductivity.

We believe such fine grain size is caused by the geometry confinement of nanofiber, which has rather small diameter itself in the range of 200 nm that may constrain the grain growth. To verify this hypothesis, we also electrospun $NaCo_2O_4$ nanofibrous mats consisting of massive nanofibers using mixed water and methanol as solvent, as shown in Figure 4. The as-spun mat

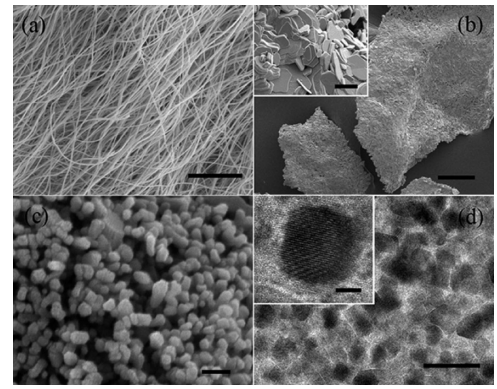

Figure 4. Microscopic images of electrospun nanofibrous mat; (a) SEM image of as-spun nanofiberous mat before annealing (scale bar represents 10 μm); and SEM images of nanofiberous mat annealed at 750 °C for two hours (b) and 10 min (c); and (d) TEM image of nanofiberous mat annealed at 750 °C for 10 min; scale bar in (b) represents 50 μm, and 5 μm in the insert of (b); scale bar in (c) represents 100 nm; scale bar in (d) represents 50 nm, and 5 nm in the insert of (d).

before annealing has nice fibrous morphology, clearly seen in SEM image in part a of Figure 4. However, because the nanofibers are intimately in contact with their neighbors, and geometry confinement of a individual nanofiber is lost. As a result, the fibrous morphology is completely lost after annealing at 750 °C for 2 h, as shown in SEM image in part b of Figure 4. The higher magnification image in the insert further shows a clear lamellar polycrystalline structure, with grain size in the range of micro meters, indicating substantial grain growth in the absence of geometric confinement. To understand such grain growth, we also examine nanofiberous mat annealed at 750 °C for just 10 min, and the SEM image in part c of Figure 4 shows a particulate instead of fibrous morphology, with particle size close to 10 nm. The TEM image in part d of Figure 4 further confirms that each of the particles is a single crystalline grain. This suggests that, while the grains grow in 3D initially, such growth is quickly dominated by lateral growth that results in lamellar grain morphology. Clearly, it is important to control the annealing time while maintaining geometric confinement to obtain nanocrystalline $NaCo_2O_4$ nanofibers with fine grain size.

The electrical conduction of a single $NaCo_2O_4$ nanofiber synthesized using water solvent is examined by conductive atomic force microscopy (cAFM) using the conductive cantilever tip as the top electrode, making it possible to map the current distribution over the nanofiber surface. The nanofiber was deposited on a Si/SiO_2 substrate that was partially coated with Pt as the bottom electrode, and the fiber spanning over both Pt and SiO_2 areas, as schematically shown in part a of Figure 5. Under such a configuration, the conductive path is shortest when the tip scans nanofiber right above Pt bottom electrode, and gradual increases when the tip moves away from the Pt electrode. This should results in higher currents closer to the Pt bottom electrode, which is indeed reflected in the current mapping shown in part b of Figure 5. The current is highest for nanofiber segment on top of Pt electrode, and gradually decreases for the nanofiber segment away from the Pt, because of the increased current path and thus larger resistance. Detailed current mappings for fiber segments over Pt and SiO_2 areas are shown in parts c and d of Figure 5, along with respective cross-section line scan of current distribution and nanofiber topography. It is observed that the current is in the range of nA for nanofiber segment above Pt electrode but drops to 10 pA range

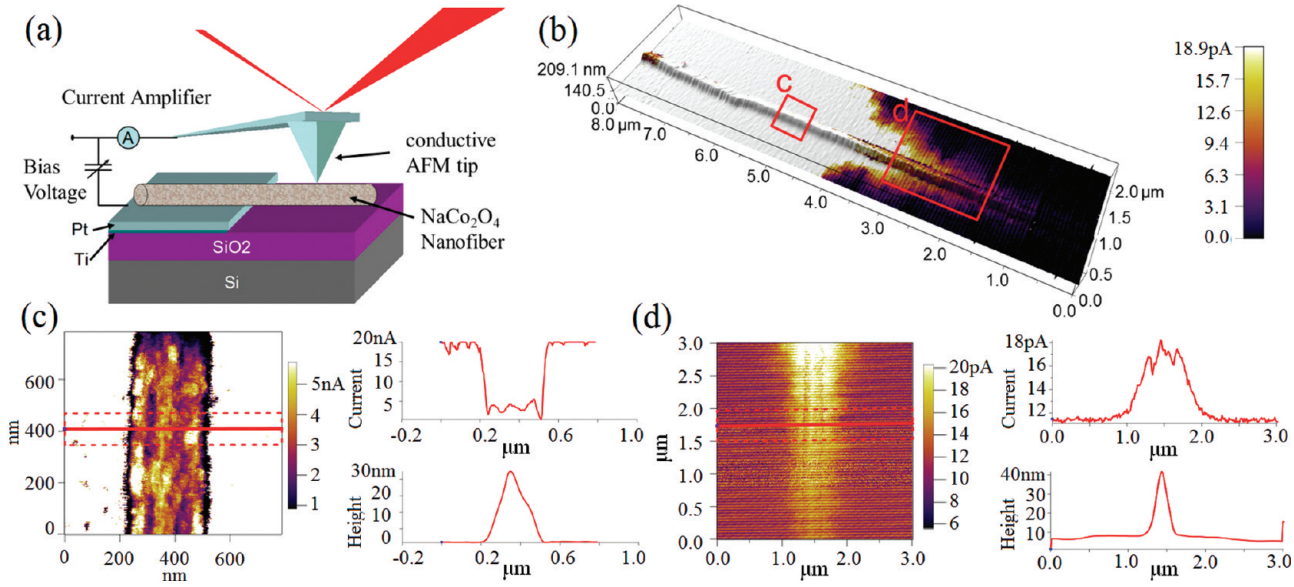

Figure 5. Mapping of electric current on $NaCo_2O_4$ nanofiber; (a) schmatic of conductive AFM; (b) current mapping of nanofiber segment on the edge between Pt and SiO_2 area, imposed on its 3D topography; (c) and (d) detailed current mapping of nanofiber segment on Pt bottom electrode (c), and on a SiO_2 area (d), with corresponding line scan of current distribution and topography.

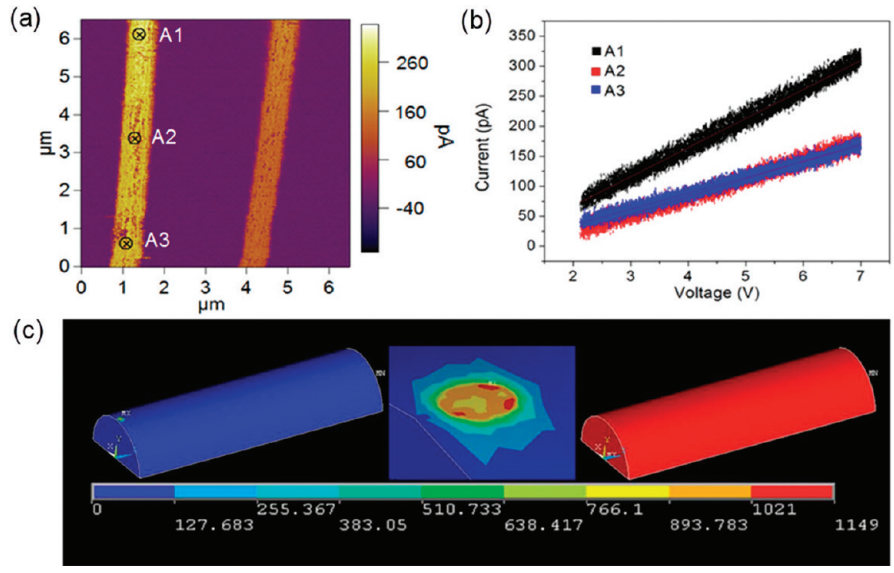

Figure 6. Electric conduction of $NaCo_2O_4$ nanofiber; (a) three points on the nanofiber where the I−V curve were measured; (b) the corresponding I−V curves from which the resistivity can be estimated; (c) finite element simulation of electric conduction in nanofiber with conductive AFM tip as top electrode (left), showing much smaller current density (A/m^2) and highly localized current distribution near AFM tip (middle), and with uniform electrodes at both ends of nanofiber (right), showing orders of magnitude higher current density.

for nanofiber segment above SiO_2 away from Pt. Nonuniform current distribution is clearly seen in part c of Figure 5, with some local high and low spots, suggesting that there are defects in the nanofiber, which may limit the overall electric conduction of nanofibers.

In order to estimate the nominal conductivity of $NaCo_2O_4$ nanofiber, we also measure local I−V curve on three spots of the nanofiber that are approximately 3 μm apart, as shown in part a of Figure 6, with A1 being closest to Pt electrode, and A3 furthest. These I−V curves are shown in part b of Figure 6, and the corresponding resistance R_i can be estimated from the slope of the curve, from which we can calculate ΔR_{ij}, the difference in resistances at points A_i and A_j. Becaise $\Delta R_{ij} = \rho(L_{ij})/(A)$, where L_{ij} is the distance between A_i and A_j and A is the cross-section area, the nominal resistivity ρ of $NaCo_2O_4$ nanofiber can be estimated. For example, choosing A1 and A3, we have $\Delta R_{13} = 1.7 \times 10^{10}\ \Omega$, $L_{13} = 5.7\ \mu$m, and $A \approx 1 \times 10^{-15}\ m^2$, from which it is estimated that $\rho \approx 2.98\ \Omega\cdot$m. If A2 and A3 are used instead, we have $\rho \approx 1.41\ \Omega\cdot$m. Other points have also been examined, resulting in similar estimate on nominal resistivity in the order of 1 $\Omega\cdot$m, which is much larger than that of bulk polycrystalline $NaCo_2O_4$. This result appears to be rather discouraging, but careful examination reveals that the AFM-based measurement substantially underestimates the conductivity of the nanofiber. To see this, we carried out finite element simulation on electric conduction in nanofiber under two different configurations, one with conductive tip as the top electrode on one end and Pt-coated substrate as the bottom electrode at the other end, and the other using uniform electrodes covering both ends of the cross-section. The resulted distributions of current density are shown in part c of Figure 6, and it is observed that due to the extremely small size of the AFM tip electrode, the overall current in the nanofiber is about two to 3 orders of magnitude smaller than that in a

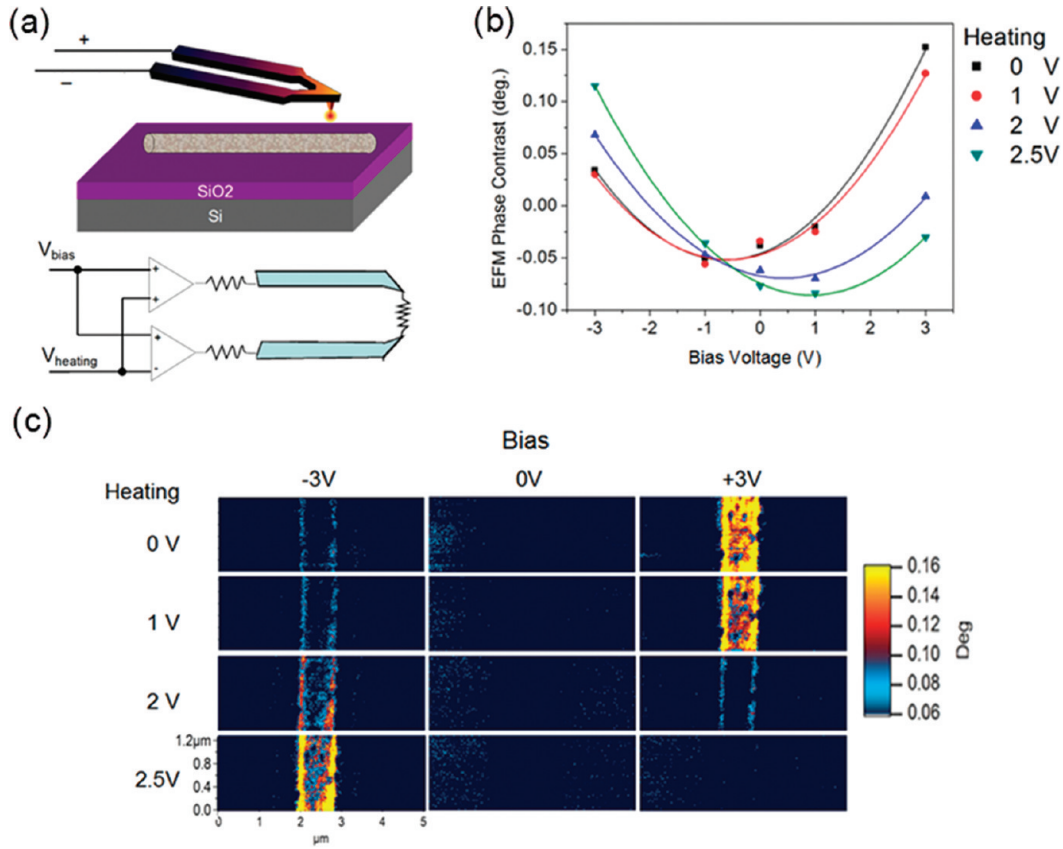

Figure 7. Thermoelectric characterization of $NaCo_2O_4$ nanofiber using scanning probe microscopy; (a) schematics of characterization; (b) EFM contrast mapping under different heating and bias voltages; (c) EFM contrast variation in $NaCo_2O_4$ nanofiber as a function of bias voltage at different heating voltages.

fiber with uniform electrodes, even though their electric conductivities are identical. Thus, if we use the cross-section area of nanofiber in calculating the nominal resistivity from the I−V curves, the electric conductivity will be substantially underestimated. In addition, substantial contact resistance exists between nanofiber and the conductive AFM tip, which will reduce the nominal conductivity even further. Thus it is not surprising or unexpected that the nominal conductivity estimated using conductive AFM tip is orders of magnitude smaller than the bulk value, and the actual conductivity of nanofiber should be much higher. Another issue that may limit the effective conductivity is defects in the nanofiber. Because of the small radius of the nanofiber, a defect would substantially lower the electric current across its cross-section. When nanofibers are consolidated into bulk ceramics, we expect that the influence of contact resistance and defects will be substantially minimized. Indeed, our recent work confirms that the nanofiber-sintered $Ca_3Co_4O_9$ ceramic has electric conductivity and power density comparable to other $Ca_3Co_4O_9$ ceramics reported in literature, yet has much reduced thermal conductivity because of its much smaller grain size, resulting in substantially enhanced thermoelectric figure of merit.[34]

To characterize the thermoelectric effect of $NaCo_2O_4$ nanofiber, a heated cantilever (ThermaLever) probe is used to heat the nanofiber locally,[35−37] as schematically shown in part a of Figure 7, by passing a heating voltage through the resistor in the probe tip. This nanoscale resistive heater increases the local temperature over several micrometers range, creating a large temperature gradient ΔT in the nanofiber, which in turn induces a large change in surface potential if the sample is thermoelectric. Such surface potential can be measured by a subsequent electrostatic force microscopy (EFM) mapping using an applied bias voltage through the conductive SPM tip. Indeed, large contrast changes in EFM phase images are observed between nanofiber and the surrounding substrate when a series of heating voltages are passed through the probe, as shown in part b of Figure 7, and such an EFM phase contrast correlates with the potential difference between the tip and sample, confirming the thermoelectric effect of the nanofiber. Furthermore, the EFM phase contrast is expected to be quadratic to the bias voltage, which is also what we observe in part c of Figure 7 under four different heating voltages, where the EFM phase contrast plotted is averaged over the scanned nanofiber segment shown in part b of Figure 7. This technique is particularly convenient to study the thermoelectric response of nanostructures wherein the scaling law works favorably, since gigantic local temperature gradient can be induced by the tiny SPM probe, similar to the large current concentration near conductive SPM tip shown in part c of Figure 6. Notice that at continuum level, the governing equations for current and thermal transports are identical in mathematical structure, and thus the finite element simulation in part c of Figure 5 can also be used to illustrate the temperature gradient near the heated SPM tip.

4. Conclusions

In summary, we have developed a sol−gel-based electrospinning technique to synthesize thermoelectric $NaCo_2O_4$ nanofiber with grain size as small as 10 nm, orders of magnitude smaller than that of sol−gel powders processed by conventional techniques. A series of scanning probe microscopy (SPM) studies have been carried out to characterize the electric conduction in a single $NaCo_2O_4$ nanofiber, and its seemly high

nominal electric resistivity is attributed to the SPM-based measurement configuration instead of intrinsically low electric conductivity. The thermoelectric effect of a single $NaCo_2O_4$ nanofiber has also been characterized by electrostatic force microscopy (EFM) in combination with a novel thermal probe.

Acknowledgment. The work is supported by National Science Foundation (CMMI-0969543) and Natural Science Foundation of China (10732100). The Asylum Research MFP-3D Atomic Force Microscope was acquired through an ARO DURIP grant (W911NF-08-01-0262). The SEM and TEM were carried out at University of Washington NanoTech User Facility, a member of the National Nanotechnology Infrastructure Network supported by National Science Foundation. Y.M.L. also acknowledges partial support from University of Washington Center for Nanotechnology UIF Fellowship, and S.H.X. acknowledges partial support of China Scholarship Council (No: 2009843269).

References and Notes

(1) Arunachalam, V. S.; Fleischer, E. L. *MRS Bull.* **2008**, *33*, 264–276.
(2) Yang, J. H.; Caillat, T. *MRS Bull.* **2006**, *31*, 224–229.
(3) DiSalvo, F. J. *Science* **1999**, *285*, 703–706.
(4) Tritt, T. M.; Subramanian, M. A. *MRS Bull.* **2006**, *31*, 188–194.
(5) Broido, D. A.; Reinecke, T. L. *Phys. Rev. B* **1995**, *51*, 13797–13800.
(6) Linchung, P. J.; Reinecke, T. L. *Phys. Rev. B* **1995**, *51*, 13244–13248.
(7) Venkatasubramanian, R.; Siivola, E.; Colpitts, T.; O'Quinn, B. *Nature* **2001**, *413*, 597–602.
(8) Harman, T. C.; Taylor, P. J.; Walsh, M. P.; LaForge, B. E. *Science* **2002**, *297*, 2229–2232.
(9) Rao, A. M.; Ji, X. H.; Tritt, T. M. *MRS Bull.* **2006**, *31*, 218–223.
(10) Bottner, H.; Chen, G.; Venkatasubramanian, R. *MRS Bull.* **2006**, *31*, 211–217.
(11) Heremans, J. P.; Jovovic, V.; Toberer, E. S.; Saramat, A.; Kurosaki, K.; Charoenphakdee, A.; Yamanaka, S.; Snyder, G. J. *Science* **2008**, *321*, 554–557.
(12) Hochbaum, A. I.; Chen, R. K.; Delgado, R. D.; Liang, W. J.; Garnett, E. C.; Najarian, M.; Majumdar, A.; Yang, P. D. *Nature* **2008**, *451*, 163–U5.
(13) Boukai, A. I.; Bunimovich, Y.; Tahir-Kheli, J.; Yu, J. K.; Goddard, W. A.; Heath, J. R. *Nature* **2008**, *451*, 168–171.
(14) Yang, Y. A.; Taggart, D. K.; Brown, M. A.; Xiang, C. X.; Kung, S. C.; Yang, F.; Hemminger, J. C.; Penner, R. M. *ACS Nano* **2009**, *3*, 4144–4154.
(15) Liu, Y. S.; Chen, Y. R.; Chen, Y. C. *ACS Nano* **2009**, *3*, 3497–3504.
(16) Snyder, G. J.; Toberer, E. S. *Nat. Mater.* **2008**, *7*, 105–114.
(17) Abramson, A. R.; Kim, W. C.; Huxtable, S. T.; Yan, H. Q.; Wu, Y. Y.; Majumdar, A.; Tien, C. L.; Yang, P. D. *J. Microelectromech. Syst.* **2004**, *13*, 505–513.
(18) Mi, J. L.; Zhao, X. B.; Zhu, T. J.; Tu, J. P. *J. Inorg. Mater.* **2008**, *23*, 715–718.
(19) Ebling, D. G.; Jacquot, A.; Jagle, M.; Bottner, H.; Kuhn, U.; Kirste, L. *Phys. Status Solidi RRL* **2007**, *1*, 238–240.
(20) Chatterjee, S. *Mater. Lett.* **2008**, *62*, 707–710.
(21) Zhou, M.; Li, J. F.; Kita, T. *J. Am. Chem. Soc.* **2008**, *130*, 4527–4532.
(22) Poudel, B.; Hao, Q.; Ma, Y.; Lan, Y. C.; Minnich, A.; Yu, B.; Yan, X.; Wang, D. Z.; Muto, A.; Vashaee, D.; Chen, X. Y.; Liu, J. M.; Dresselhaus, M. S.; Chen, G.; Ren, Z. *Science* **2008**, *320*, 634–638.
(23) Xie, S. H.; Li, J. Y.; Liu, Y. Y.; Lan, L. N.; Jin, G.; Zhou, Y. C. *J. Appl. Phys.* **2008**, *104*, 024115.
(24) Xie, S. H.; Li, J. Y.; Proksch, R.; Liu, Y. M.; Zhou, Y. C.; Liu, Y. Y.; Ou, Y.; Lan, L. N.; Qiao, Y. *Appl. Phys. Lett.* **2008**, *93*, 222904.
(25) Xie, S. H.; Li, J. Y.; Qiao, Y.; Liu, Y. Y.; Lan, L. N.; Zhou, Y. C.; Tan, S. T. *Appl. Phys. Lett.* **2008**, *92*, 062901.
(26) Maensiri, S.; Nuansing, W. *Mater. Chem. Phys.* **2006**, *99*, 104–108.
(27) Koumoto, K.; Terasaki, I.; Funahashi, R. *MRS Bull.* **2006**, *31*, 206–210.
(28) Julien, M. H.; de Vaulx, C.; Mayaffre, H.; Berthier, C.; Horvatic, M.; Simonet, V.; Wooldridge, J.; Balakrishnan, G.; Lees, M. R.; Chen, D. P.; Lin, C. T.; Lejay, P. *Phys. Rev. Lett.* **2008**, *100*, 096405.
(29) Kobayashi, W.; Hebert, S.; Pelloquin, D.; Perez, O.; Maignan, A. *Phys. Rev. B* **2007**, *76*, 245102.
(30) Limelette, P.; Hardy, V.; Auban-Senzier, P.; Jerome, D.; Flahaut, D.; Hebert, S.; Fresard, R.; Simon, C.; Noudem, J.; Maignan, A. *Phys. Rev. B* **2005**, *71*, 233108.
(31) Terasaki, I.; Tanaka, H.; Satake, A.; Okada, S.; Fujii, T. *Phys. Rev. B* **2004**, *70*, 214106.
(32) Fujita, K.; Mochida, T.; Nakamura, K. *Jpn. J. Appl. Phys., Part 1* **2001**, *40*, 4644–4647.
(33) Ito, M.; Nagira, T.; Furumoto, D.; Katsuyama, S.; Nagai, H. *Scr. Mater.* **2003**, *48*, 403–408.
(34) Yin, T. F.; Liu, D. W.; Ou, Y.; Ma, F. Y.; Xie, S. H.; Li, J. F.; Li, J. Y. *J. Phys. Chem. C* **2010**, *114*, 10061–10065.
(35) Remmert, J. L.; Wu, Y.; Lee, J. C.; Shannon, M. A.; King, W. P. *Appl. Phys. Lett.* **2007**, *91*, 143111.
(36) Dai, Z.; King, W. P.; Park, K. *Nanotechnology* **2009**, *20*, 095301.
(37) Lee, J.; Liao, A.; Pop, E.; King, W. P. *Nano Lett.* **2009**, *9*, 1356–1361.

JP107488K